nature neuroscience

K-ATP channels promote the differential degeneration of dopaminergic midbrain neurons

Birgit Liss[1–3], Olga Haeckel[1], Johannes Wildmann[4], Takashi Miki[5], Susumu Seino[5] & Jochen Roeper[2,6]

The selective degeneration of dopaminergic (DA) midbrain neurons in the substantia nigra (SN) is a hallmark of Parkinson disease. DA neurons in the neighboring ventral tegmental area (VTA) are significantly less affected. The mechanisms for this differential vulnerability of DA neurons are unknown. We identified selective activation of ATP-sensitive potassium (K-ATP) channels as a potential mechanism. We show that in response to parkinsonism-inducing toxins, electrophysiological activity of SN DA neurons, but not VTA DA neurons, is lost owing to activation of K-ATP channels. This selective K-ATP channel activation is controlled by differences in mitochondrial uncoupling between SN and VTA DA neurons. Genetic inactivation of the K-ATP channel pore-forming subunit Kir6.2 resulted in a selective rescue of SN but not VTA DA neurons in two mechanistically distinct mouse models of dopaminergic degeneration, the neurotoxicological 1-methyl-4-phenyl-1,2,3,6-tetrahydropyridine (MPTP) model and the mutant *weaver* mouse. Thus, K-ATP channel activation has an unexpected role in promoting death of DA neurons in chronic disease.

Differential vulnerability of neuronal populations to cell death is found in most neurodegenerative diseases[1]. In Parkinson disease, this differential vulnerability is particularly notable within the clinically most relevant population of dopaminergic (DA) midbrain neurons. Here, highly vulnerable DA subpopulations within the substantia nigra (SN) and their axonal projections to dorsal parts of the striatum are almost completely lost, whereas neighboring DA subpopulations within the ventral tegmental area (VTA) and their projections to ventral striatum survive to a large extent[2]. For rare forms of familial Parkinson disease, several causal gene mutations have been identified[3,4], but as their respective gene products are ubiquitously expressed, they alone do not explain the selective pattern of DA cell loss. For the common sporadic form of Parkinson disease, diverse candidate mechanisms have been discussed, including mitochondrial dysfunction, oxidative stress and proteasomal impairment[4–6]. However, as the stereotypical pattern of differential cell loss of DA neurons is reproduced in mechanistically distinct Parkinson disease animals models[2,5,7,8], different toxic and molecular pathways might converge on a common but still unknown cellular mechanism for differential neuronal vulnerability[3,9].

One well-described cellular stressor in Parkinson disease and its animal models is mitochondrial dysfunction; SN neurons from Parkinson disease patients show reduced activity of complex I of the mitochondrial respiratory chain[6]. Accordingly, the neurotoxic complex I inhibitors rotenone and MPP+ (1-methyl-4-phenylpyridinium, the active metabolite of MPTP)[5] induce differential degeneration of DA neurons and parkinsonism in animals[9–11] as well as in humans[7,12]. The relative importance of the various downstream consequences of reduced mitochondrial complex I activity for neurodegeneration is not fully understood; complex I inhibition might reduce mitochondrial ATP production and in turn could compromise proteasomal activity[13]. Equally important, complex I inhibition could increase production of reactive oxygen species (ROS), which in turn elevate oxidative stress and the load of misfolded proteins[14]. How these immediate biochemical consequences of complex I inhibition are translated into cell-specific pathophysiology and eventually result in differential cell death of DA neurons is unknown.

Here, we investigated the role of a potential downstream target of complex I inhibition, the K-ATP channel. These channels, composed of discrete pore-forming (Kir6.1/Kir6.2) and regulatory subunits (SUR1/SUR2), are called 'metabolic sensors', as their open probability depends on the metabolic state of a cell[15–17]. K-ATP channels in dopaminergic neurons have been shown to open in response to partial complex I inhibition as well as in response to ATP depletion and increased oxidative stress (ROS)[18–20]. Thus, cell type–specific K-ATP channel activation would provide a convergent downstream target that could integrate energy depletion and oxidative stress, offering a candidate mechanism for the differential vulnerability of DA neurons in Parkinson disease.

RESULTS

Identification of mesostriatal and mesolimbic DA neurons

To investigate differential vulnerability in the mature dopaminergic midbrain with single-cell resolution, we combined *in vitro*

[1]Molecular Neurobiology, Department of Physiology, Marburg University Deutschhausstrasse 2, 35037 Marburg, Germany. [2]MRC Anatomical Neuropharmacology Unit, Oxford University, Mansfield Road, Oxford OX1 3TH, UK. [3]University Laboratory of Physiology, Oxford University, Parks Road, Oxford OX1 3PT, UK. [4]Immunology, Department of Physiology, Marburg University, Deutschhausstrasse 2, 35037 Marburg, Germany. [5]Cellular and Molecular Medicine, University Graduate School of Medicine, 7-5-1 Kusunoki-cho, 650-0017 Kobe, Japan. [6]Neurophysiology, Department of Physiology, Marburg University, Deutschhausstrasse 2, 35037 Marburg, Germany. Correspondence should be addressed to B.L. (birgit.liss@staff.uni-marburg.de).

Received 25 July; accepted 19 September; published online 20 November 2005; doi:10.1038/nn1570

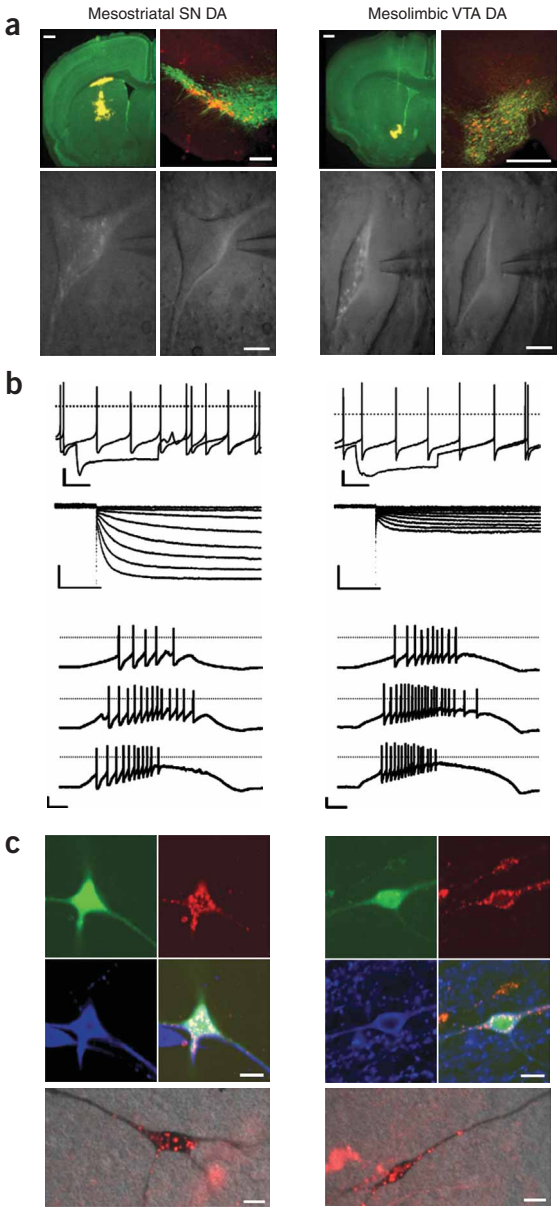

Figure 1 Properties of adult mesostriatal and mesolimbic DA neurons. (**a**) Identification of mesostriatal and mesolimbic DA neurons. For both images of SN neurons (left) and images of VTA neurons (right), upper left image shows injection sites (striatum for SN and nucleus accumbens for VTA, scale bars, 400 μm), upper right image shows midbrain localization of TH-positive (green) and retrobead-labeled (red) neurons (scale bars, 150 μm), and the lower row shows identification of retrobead-labeled SN und VTA neurons in living brain slices via infrared videomicroscopy and epifluorescence (scale bars, 5 μm). (**b**) Electrophysiological properties of retrogradely labeled mesostriatal and mesolimbic DA neurons. Upper row: spontaneous activities and responses to −100 pA current injection (scale bars: 20 mV, 400 ms; dashed line, 0 mV). Middle row: activation of I_h currents by hyperpolarizing voltage steps (10-mV increments) from −40 mV (scale bars: 200 pA, 400 ms). Bottom row: responses to 50 pA, 250 pA and 500 pA current ramps from SN and VTA DA neurons (scale bars: 20 mV, 400 ms). (**c**) Upper images: confocal analysis of traced (red), recorded and neurobiotin-filled (green), and TH-positive (blue) neurons. Lower images: morphology of traced, neurobiotin-filled and DAB-processed TH-positive neurons (scale bars, 10 μm).

electrophysiology, gene expression profiling and immunohistochemistry of individual retrogradely labeled mesostriatal SN and mesolimbic VTA DA neurons in adult mice[21]. **Figure 1a** shows injection sites of retrograde tracer substances in dorsal striatum and nucleus accumbens; distribution of labeled mesostriatal and mesolimbic TH-positive cell bodies within SN and VTA (upper panels); and single, fluorescently labeled mesostriatal and mesolimbic neurons in living brain-slices from 3-month-old mice (lower panels). Adult fluorescence-labeled DA neurons showed typical electrophysiological properties (such as spontaneous pacemaker activity, broad action potentials and presence of hyperpolarization-activated current (I_h)–mediated sag components (**Fig. 1b**)) similar to those described for 14-d-old postnatal unlabeled DA neurons[22]. Physiological differences between DA midbrain neurons, such as differences in sag and I_h current amplitudes and maximal firing rates before onset of depolarization block, were associated with distinct DA projections to striatal or accumbal target areas (**Fig. 1b**; sag amplitudes at –100 mV: mesostriatal, 16.5 ± 0.9 mV, $n = 15$; mesolimbic, 12.0 ± 1.2 mV, $n = 10$; $P < 0.01$; I_h amplitudes at –120 mV: mesostriatal, 255 ± 46 pA, $n = 15$; mesolimbic, 60 ± 15 pA, $n = 10$; $P < 0.01$; maximum firing rate: mesostriatal, 8.3 ± 2.0 Hz, $n = 15$; mesolimbic, 13.8 ± 3.0 Hz, $n = 10$; $P < 0.01$). Functionally characterized, labeled neurons were filled with neurobiotin during whole-cell recordings (or by breaking into whole-cell mode after perforated-patch recordings) for subsequent triple labeling immunohistochemistry in order to confirm their dopaminergic identity (as measured by tyrosine hydroxylase (TH) expression) and morphology (**Fig. 1c**).

All DA midbrain neurons express functional K-ATP channels

The presence of K-ATP channels in postnatal DA neurons is well described[18,20,23,24], but potential differences between adult mesolimbic VTA and mesostriatal SN DA neurons have not yet been addressed. To probe for the presence of functional K-ATP channels, we dialyzed DA neurons in brain slices with ATP-free pipette solution. Our previous data suggested that Kir6.2 (KCNJ11) is the pore-forming subunit of K-ATP channels in all DA midbrain neurons[18,25]. Therefore, we also analyzed DA neurons of a K-ATP channel knockout (Kir6.2$^{-/-}$) mouse in which the Kir6.2 gene was disrupted[15,26]. K-ATP currents were activated in both mesostriatal SN and, to a smaller degree, mesolimbic VTA DA neurons from adult wild-type (Kir6.2$^{+/+}$) mice (**Fig. 2a**). The washout-induced current at –50 mV was 112.4 ± 16.3 pA for mesostriatal DA neurons ($n = 10$) and 56.4 ± 16.9 pA for mesolimbic DA neurons ($n = 12$). The activation of K-ATP channels in DA neurons was accompanied by hyperpolarization of the membrane potential below threshold (for mesostriatal DA neurons, –35.6 ± 1.8 mV for the control condition ($n = 10$) and –51.9 ± 2.6 mV for the ATP washout condition ($n = 10$); and for mesolimbic DA neurons, –35.5 ± 1.1 mV for the control condition ($n = 12$) and –49.1 ± 5.2 mV ($n = 12$) for the ATP washout condition). In contrast to results from wild-type mice, no K-ATP currents were activated in response to zero ATP dialysis in Kir6.2$^{-/-}$ mice, nor did we observe any hyperpolarization in mesolimbic or mesostriatal DA neurons in Kir6.2$^{-/-}$ mice. The mean current difference after washout at –50 mV was –8.0 ± 14.3 pA for mesostriatal DA neurons ($n = 6$) and 7.2 ± 3.4 pA for mesolimbic DA neurons ($n = 6$). Basic electrophysiological properties of single action potentials and spontaneous discharge rates, recorded in the perforated-patch configuration at physiological temperatures and glucose concentrations, did not differ significantly in DA neurons from adult Kir6.2$^{-/-}$ mice and wild-type mice (**Fig. 2b**). The action potential width for Kir6.2$^{+/+}$ mice was 3.1 ± 0.34 ms ($n = 12$) and for Kir6.2$^{-/-}$ mice, 2.9 ± 0.24 ms ($n = 10$). The spontaneous activity for Kir6.2$^{+/+}$

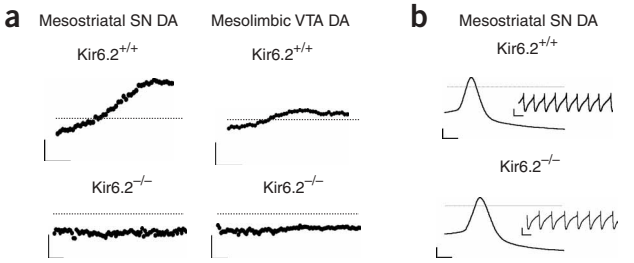

Figure 2 Kir6.2 forms the K-ATP channel pore in all DA neurons. (**a**) Current amplitudes during ATP washout (at −50 mV) in mesostriatal and mesolimbic DA neurons from Kir6.2$^{+/+}$ and Kir6.2$^{-/-}$ mice (scale bars: 50 pA, 100 ms, dashed line, 0 pA). (**b**) Single action potentials and spontaneous discharges (insert) of Kir6.2$^{+/+}$ and Kir6.2$^{-/-}$ SN DA neurons recorded in the perforated-patch configuration.

mice was 1.75 ± 0.20 Hz (n = 36) and 2.03 ± 0.20 Hz for Kir6.2$^{-/-}$ mice (n = 15). These data are in accordance with our previous study on young postnatal mice and demonstrate that Kir6.2 is the essential pore-forming subunit for functional somatodendritic K-ATP channels in mesostriatal as well as mesolimbic DA neurons from adult mice.

Distinct molecular compositions of K-ATP channels might confer variable metabolic sensitivities to native channels[16]. Thus, we analyzed K-ATP channel subunit expression of individual SN and VTA DA neurons using RT-PCR. We have previously shown that in young mice (postnatal day 14 (P14)), K-ATP channels in DA midbrain neurons coexpressed Kir6.2 and SUR1 or SUR2B mRNA[18]. As previously described for rotenone[18], DA neurons expressing SUR1 mRNA, but not SUR2B mRNA, from P14 mice underwent K-ATP channel activation after acute application of 1-methyl-4-phenylpyridinium (MPP+). Hyperpolarization to –53.8 ± 2.4 mV (n = 7) was induced; six out of these seven neurons expressed SUR1. This confirmed SUR1-containing K-ATP channels as metabolic sensors in DA neurons. To study K-ATP channel subunit expression in adult mice, DA neurons (identified by fluorescence labeling) were harvested by means of photoablation and laser microdissection (**Fig. 3**). Notably, in microdissected DA neurons from adult mice, we found no evidence for differential expression of SUR subunits. Using qualitative RT-PCR, we detected SUR1 mRNA with similar frequencies in single SN and VTA DA neurons but detected SUR2B mRNA in <5% of individual DA neurons (**Fig. 3a**,**b**): 36% of SN neurons (9/25), and 41.6% of VTA neurons (n = 10/24), were SUR1- and TH-positive. In contrast to the SUR isoforms, and in accordance with previous studies, mRNA for calbindin, a marker for more resistant DA neurons, was coexpressed to a higher degree in VTA DA neurons (62.5%, or 15/24) than in SN DA neurons (4%, or 1/25, **Fig. 3b**).

Figure 3 K-ATP subunit expression of individual laser-microdissected DA neurons. (**a**) Qualitative RT-PCR of individual laser-microdissected SN and VTA DA neurons. Top: detection of a retrobead-labeled mesolimbic VTA neuron (scale bar, 5 μm). Blue arrowhead is an adjustment symbol of laser software. Bottom: mRNA expression profiles of a single mesostriatal SN and a single mesolimbic VTA neuron. (**b**) Calbindin is more frequently detected in single VTA DA compared to SN DA neurons. (**c**) Top: photomicrograph of a section after laser microdissection of selective VTA and SN cell pools for quantitative PCR (scale bar, 100 μm). Bottom: qualitative PCR with one-tenth aliquot of cDNA reaction from a VTA DA cell pool illustrates absence of glial (GFAP) or GABAergic (GAD65/GAD67) contamination (see Methods). Blue arrowhead as in **a**. (**d**) Quantitative real-time PCR. There are significantly higher mRNA expression (normalized to mean SN expression) of SUR1 in cell pools of SN DA neurons than in VTA DA neurons.

Quantitative real-time PCR of homogeneous microdissected SN DA and VTA DA cell pools (ten neurons) for all four K-ATP channel subunits eliminated detection threshold problems and confirmed that Kir6.2 and SUR1, not Kir6.1 or SUR2, are the relevant K-ATP channel subunits in SN DA neurons as well as in VTA DA neurons from adult mice. (Detection frequencies were 100% for SUR1 and Kir6.2, <10% for SUR2, and 0% for Kir6.1.) Relative levels of SUR1 mRNA expression were about twofold higher in SN DA neurons than in VTA DA neurons, consistent with the twofold-larger K-ATP washout currents of mesostriatal SN DA neurons (**Fig. 3d**). (SUR1 expression was 100 ± 16.9 in SN (n = 11) and 45.1 ± 5.5 in VTA (n = 8; P = 0.009). Kir6.2 expression was 100 ± 21.5 in SN (n = 10) and 51.8 ± 12.4 in VTA (n = 8; P = 0.07). Mean SN expression was normalized to 100.) Thus, K-ATP channels have a uniform molecular makeup but distinct mRNA expression levels across DA midbrain populations. However, K-ATP subunit composition or expression levels alone do not determine the metabolic sensitivity of K-ATP channels in intact neurons, as K-ATP channel gating is controlled by the intracellular ATP/ADP ratio and is regulated by a number of complex signaling factors, such as reactive oxygen species, phosphorylation, phosphoinositides and long-chain acyl-CoA esters[27–30].

Complex I inhibition selectively activates K-ATP channels

To avoid perturbation of cellular metabolism, we studied sensitivities of K-ATP channel activation in DA neurons in response to the complex I inhibitors and neurotoxins rotenone and MPP+ in the perforated-patch configuration at physiological temperatures and glucose concentrations.

In mesostriatal SN DA neurons from adult Kir6.2$^{+/+}$ mice, application of MPP+ (10 μM for 5 min) induced a slowing followed by a complete cessation of spontaneous activity (n = 14/15) and a tonic hyperpolarization (**Fig. 4a**,**b**; control: 1.7 ± 0.2 Hz, −44.7 ± 1.2 mV, n = 15; post-MPP+: 0.1 ± 0.1 Hz, −61.3 ± 1.5 mV, n = 15; $P = 1.6 \times 10^{-8}$, $P = 5.3 \times 10^{-4}$). By contrast, spontaneous activities and membrane potentials of mesolimbic DA neurons were not significantly affected by 10 μM MPP+ (control: 2.4 ± 0.4 Hz, −42.7 ± 3.5 mV, n = 6; post-MPP+: 2.3 ± 1.1 Hz, –40.7 ± 4.9 mV, n = 6). In Kir6.2$^{-/-}$ mice,

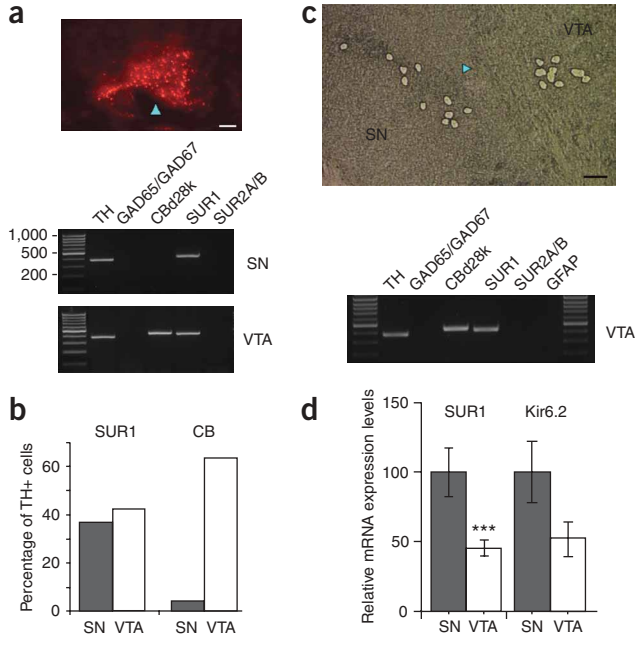

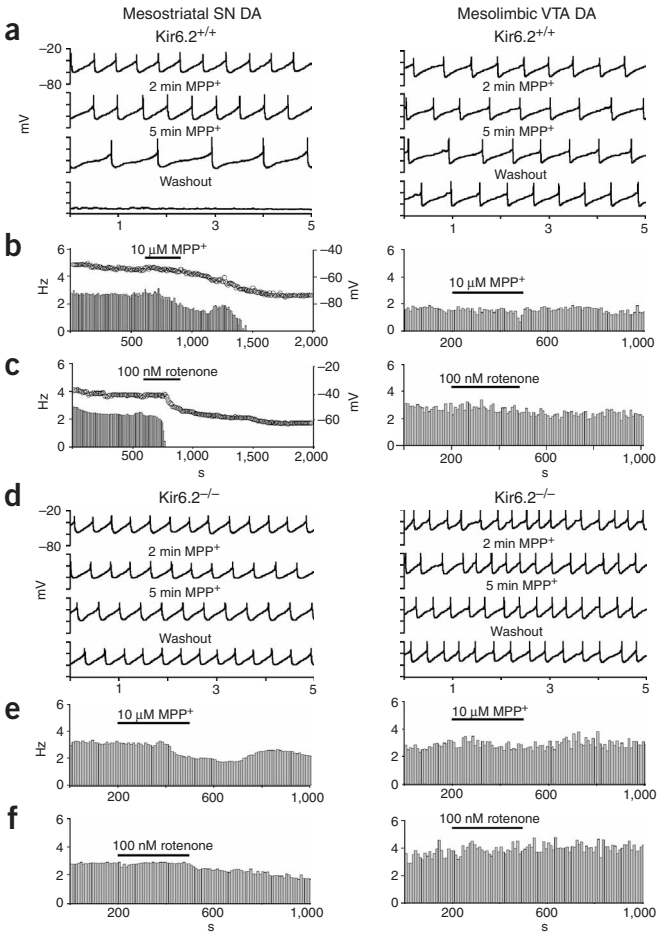

Figure 4 K-ATP channel activation in response to complex I inhibition only in SN DA neurons. (**a**,**d**) Spontaneous activities and responses to 10 µM MPP+ in DA neurons from Kir6.2$^{+/+}$ and Kir6.2$^{-/-}$ mice (current-clamp, perforated-patch recordings in adult brain slices at 36 °C). (**b**,**e**) Spontaneous firing frequencies (Hz/10 s bins) and mean membrane potential (mV) (horizontal bars indicate MPP+ application). (**c**,**f**) Corresponding experiments with 100 nM rotenone (horizontal bars indicate rotenone application).

neither mesostriatal SN DA nor mesolimbic VTA DA neurons showed MPP+-induced silencing of spontaneous activity (**Fig. 4d**,**e**; mesostriatal: control, 2.0 ± 0.2 Hz, −44.3 ± 0.6 mV, $n = 6$; post-MPP+, 1.8 ± 0.2 Hz, −43.9 ± 1.0 mV, $n = 6$; mesolimbic: control, 2.6 ± 1.0 Hz, −42.5 ± 1.1 mV, $n = 6$; post-MPP+, 2.7 ± 1.0 Hz, −41.7 ± 1.3 mV, $n = 6$). We also observed selective silencing of mesostriatal but not mesolimbic Kir6.2$^{+/+}$ DA neurons in response to 100 nM rotenone (**Fig. 4c**; mesostriatal: control, 1.8 ± 0.2 Hz, −44.1 ± 2.4 mV; post-rotenone, 0.0 ± 0.1 Hz, −61.3 ± 1.5 mV, $n = 12$; $P = 3.3 \times 10^{-5}$, $P = 4.5 \times 10^{-5}$; mesolimbic: control, 3.8 ± 1.1 Hz, −42.1 ± 3.4 mV; post-rotenone, 4.3 ± 1.1 Hz, –39.8 ± 5.1 mV, $n = 6$). Again, activity of Kir6.2$^{-/-}$ DA neurons was not significantly altered by rotenone (**Fig. 4f**; mesostriatal: control, 1.9 ± 0.3 Hz, −44.1 ± 1.5 mV; post-rotenone, 1.9 ± 0.4 Hz, −44.2 ± 1.7 mV, $n = 9$; mesolimbic: control, 3.9 ± 1.0 Hz, –42.8 ± 2.1 mV; post-rotenone, 3.8 ± 1.2 Hz, −43.4 ± 2.3 mV, $n = 6$).

These data demonstrate that complex I inhibition induces selective hyperpolarization and electrical silencing of highly vulnerable mesostriatal SN DA neurons, but not VTA DA neurons, owing to activation of K-ATP channels made up of Kir6.2 and SUR1 subunits. As rotenone uptake (in contrast to MPP+ uptake) is passive, the differential responses of mesostriatal and mesolimbic DA neurons are independent of toxin loading effects.

Mitochondrial uncoupling controls K-ATP channel activation

As K-ATP channels in all DA neurons are composed of Kir6.2 and SUR1 subunits, other factors (including differences in ATP consumption or ATP generation) must cause the observed differential channel activation in response to complex I inhibition. Extensive uncoupling of the mitochondrial respiratory chain by 2 µM carbonyl-cyanide-4-trifluoromethoxyphenylhydrazone (FCCP) activated K-ATP channels in both SN DA and VTA DA neurons (perforated-patch recording in 2 µM FCCP; SN: 0 ± 0 Hz, −75.8 ± 1.1 mV; VTA: 0 ± 0 Hz, −64.8 ± 9.0 mV, $n = 3$; $P = 0.35$). This indicates that K-ATP channel gating is primarily controlled by mitochondrial metabolism in all DA midbrain neurons. Consequently, quantitative differences in mitochondrial uncoupling might cause the differential sensitivity of K-ATP channels to complex I inhibition. Thus, we studied the effects of mild uncoupling of the mitochondrial respiratory chain induced by 50 nM FCCP. Mild neuronal uncoupling reduces the generation of reactive oxygen species (ROS) rather than impairing ATP production[31,32]. We found that 50 nM FCCP (20-min preincubation) alone did not activate K-ATP channels or alter firing rates of SN or VTA DA neurons (**Fig. 5a**; perforated-patch recording in 50 nM FCCP; SN: 1.9 ± 0.2 Hz, $n = 10$; VTA: 2.4 ± 0.5 Hz, $n = 6$). Notably, however, mild uncoupling inverted the response of K-ATP channels to complex I inhibition: in this case, VTA DA neurons, but not SN DA neurons, were hyperpolarized and functionally silenced due to K-ATP channel activation. In the presence of 50 nM FCCP, none of the SN DA neurons was significantly affected by 100 nM rotenone (**Fig. 5a**,**b**, left; perforated-patch recording in 50 nM FCCP: 2.33 ± 0.29 Hz; FCCP + rotenone: 1.92 ± 0.36, $n = 6$; $P = 0.40$) or 10 µM MPP+ (data not shown). In contrast, the presence of 50 nM FCCP sensitized K-ATP channels of VTA DA neurons to complex I inhibition (**Fig. 5a**,**b**, right; 50 nM FCCP: 2.4 ± 0.55 Hz; FCCP + rotenone: 0 ± 0 Hz, $n = 6$; $P = 0.0075$). We found that 50 nM FCCP had no effects on membrane conductance of DA neurons from Kir6.2$^{-/-}$ mice, in the absence or presence of rotenone (SN DA: control, 1.88 ± 0.36 nS; 50 nM FCCP, 1.95 ± 0.23 nS, $n = 6$, $P = 0.88$; VTA DA: control, 2.23 ± 0.27 nS; 50 nM FCCP, 2.07 ± 0.62 nS, $n = 3$, $P = 0.83$).

To quantify the reciprocal effects of mild uncoupling on K-ATP channel activation in response to complex I inhibition in SN and VTA DA neurons, we generated dose-response curves for rotenone-induced K-ATP channel activation in the presence and absence of 50 nM FCCP. In response to a 5-min application of rotenone (concentrations from 1–1,000 nM), the subthreshold slope conductances (G_{min}) of SN DA neurons increased fourfold to a maximum of about 7 nS (**Fig. 5c**, left; G_{base}: 1.75 ± 0.1 nS; G_{max}: 6.99 ± 0.1 nS; $n = 3$–6), but increased only about 1.8-fold to a maximum of 3.3 nS in VTA DA neurons (**Fig. 5c**, right; G_{base}: 1.78 ± 0.03 nS, G_{max}: 3.28 ± 0.03 nS; $n = 3$–6). Preincubation of SN DA neurons with 50 nM FCCP substantially reduced the sensitivity and extent of rotenone-induced K-ATP channel activation to a degree similar to that of VTA DA neurons under control conditions (**Fig. 5c**, left; control: rotenone concentration for half-maximum response (EC_{50}): 77.6 ± 3.1 nM, $G_{K\text{-}ATP}$: 5.42 nS; 50 nM FCCP: EC_{50}: 260 ± 17 nM, $G_{K\text{-}ATP}$: 1.89 nS). In contrast, in VTA DA neurons, mild uncoupling substantially potentiated rotenone-induced K-ATP channel activation (**Fig. 5c**, right; control: EC_{50}: 82.2 ± 4.3 nM, $G_{K\text{-}ATP}$: 1.50 nS; 50 nM FCCP: EC_{50}: 46.0 ± 1.8 nM, $G_{K\text{-}ATP}$: 2.62 nS). In SN DA neurons, mild uncoupling not only prevented the loss of

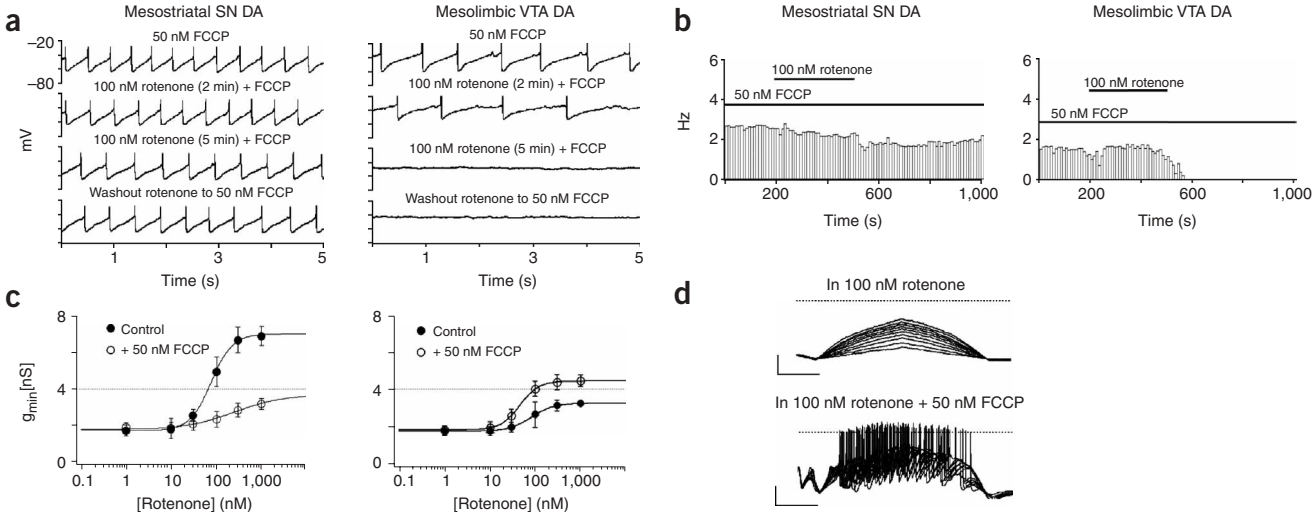

Figure 5 Mitochondrial uncoupling controls differential K-ATP channel activation. (**a**) Spontaneous activities and responses to 100 nM rotenone of SN DA and VTA DA neurons from Kir6.2$^{+/+}$ mice in the presence of 50 nM of the mitochondrial uncoupler FCCP (current-clamp, perforated-patch recordings in adult brain slices at 36 °C). (**b**) Spontaneous firing frequencies (Hz/10 s bins) of SN and VTA DA neurons in 50 nM FCCP (horizontal bars indicate rotenone application). (**c**) Rotenone concentration-dependence of minimal slope conductances (G_{min}) in SN and VTA DA neurons in the presence and absence of 50 nM FCCP. Points are mean ± s.e.m. of 3–6 experiments. Lines represent fits of the mean data by a Hill equation. (**d**) Electrophysiological properties of SN DA neurons after 5 min incubation with 100 nM rotenone in the absence (top) and presence (bottom) of 50 nM FCCP. Responses to depolarizing current ramps (50-pA steps; scale bars: 20 mV, 1 s; compare with **Fig. 1b**, lower panels).

spontaneous activity in the presence of complex I inhibition but also restored their excitability in response to current ramps (**Fig. 5d**; compare **Fig. 1b**, right panels).

In accordance with a proposed reduction of ROS rather than reduced ATP levels as the main consequence of mild uncoupling[31], preincubation of SN DA neurons with a superoxide dismutase mimetic (30 μM Mn(III)tetrakis(4-benzoic acid)porphrin chloride (MnTBAP)) also prevented rotenone-induced K-ATP channel activation and membrane hyperpolarization (100 nM rotenone + 30 μM MnTBAP: −33.68 ± 4.16 mV, 2.45 ± 0.42 nS, $n = 6$). These data could indicate that VTA DA neurons, in contrast to SN DA neurons, already show a mild degree of constitutive uncoupling of the mitochondrial respiratory chain that reduces ROS and in turn prevents K-ATP channel activation[20] in response to complex I inhibition. For further experimental support, using real-time quantitative RT-PCR, we quantified the mRNA expression of the two most relevant neuronal uncoupling proteins, UCP-2 and UCP-3 (ref. 31), both of which we found to be expressed in mouse brain. Consistently, we detected an about threefold-higher level of UCP-2 mRNA in laser-microdissected VTA DA neurons than in SN DA neurons. UCP-3 mRNA was not detected in DA neurons (UCP-2: SN, 100.0 ± 16.9, $n = 11$; VTA, 316.4 ± 49.8, $n = 11$; $P = 0.0014$. Mean SN expression was normalized to 100).

The EC_{50} values for K-ATP channel activation in response to chronic *in vitro* complex I inhibition (>30 min preincubation) by MPP+ (EC_{50}: 2.2 μM) and rotenone (EC_{50}: 16.2 nM; ref 18) in SN DA neurons are within the range of the effective *in vivo* toxin concentrations in their respective rodent Parkinson disease models[10,11]. Thus, our data suggest the possibility that selective K-ATP channel activation in mesostriatal SN DA is also operative *in vivo*. Notably, in this context, mild mitochondrial uncoupling or increased expression of UCP-2 *in vivo* has been shown to be neuroprotective in animal models of Parkinson disease[33,34].

Selective SN DA rescue in MPTP-treated Kir6.2$^{-/-}$ mice

To investigate whether K-ATP channels *in vivo* are responsible for the preferential degeneration of mesostriatal SN DA neurons, we compared the extent and distribution of striatal DA fiber loss and dopaminergic cell death for Kir6.2$^{+/+}$ and Kir6.2$^{-/-}$ mice in two mechanistically independent mouse models of selective dopaminergic degeneration: a chronic low-dose MPTP model of Parkinson disease[8] as well as the mutant *weaver* mouse[35].

Chronic low-dose MPTP administration replicated the differential loss of DA fibers and neurons typical of Parkinson disease (**Fig. 6**). We observed a reduction of about 70% in the density of TH-immunopositive fibers in the dorsal striatum of Kir6.2$^{+/+}$ mice, whereas projections to the ventral striatum were not significantly reduced (**Fig. 6a,b**; optical densities: dorsal striatum: control, 33.4 ± 2.6, $n = 10$; post-MPTP, 11.3 ± 1.3, $n = 6$, $P = 4.2 \times 10^{-6}$; ventral striatum: control, 17.4 ± 3.8, $n = 10$; post-MPTP, 18.0 ± 3.4, $n = 6$). In Kir6.2$^{-/-}$ controls, TH fiber density in dorsal and ventral striatum was not significantly different from that in the wild-type condition. In contrast, after chronic MPTP, TH fiber density was selectively increased by about 100% in Kir6.2$^{-/-}$ mice compared with wild-type mice, in the dorsal ($P = 0.004$) but not in the ventral striatum ($P = 0.24$; **Fig. 6a,b**; dorsal striatum: control, 33.3 ± 2.8, $n = 12$; post-MPTP, 21.6 ± 1.9, $n = 6$; $P = 0.005$; ventral striatum: control, 21.2 ± 4.5, $n = 10$; post-MPTP, 13.9 ± 2.2, $n = 6$).

The differential rescue of the mesostriatal DA system of Kir6.2$^{-/-}$ mice was even more evident in the midbrain. Based on nonbiased stereology, we quantified the number of TH-positive neurons in SN and VTA in controls and after chronic MPTP across the entire caudo-rostral extent of the midbrain (**Fig. 6c–e**). In Kir6.2$^{+/+}$ mice, MPTP-induced loss of TH-positive neurons within the SN was about 50% (control, 5,177 ± 212, $n = 5$; post-MPTP, 2,740 ± 199, $n = 9$; $P = 4.9 \times 10^{-7}$). Cell loss was more extensive in caudal sections, consistent with the caudo-rostral pattern found in Parkinson disease[2] (**Fig. 6e**, top). In the VTA, only about 25% of TH-positive cells were lost after MPTP treatment (control, 3,578 ± 175, $n = 5$; post-MPTP, 2,602 ± 70, $n = 4$; $P = 0.003$). In Kir6.2$^{-/-}$ mice, the number of TH-positive neurons in SN or VTA under control conditions was not significantly different from that in Kir6.2$^{+/+}$ mice. Also, the moderate

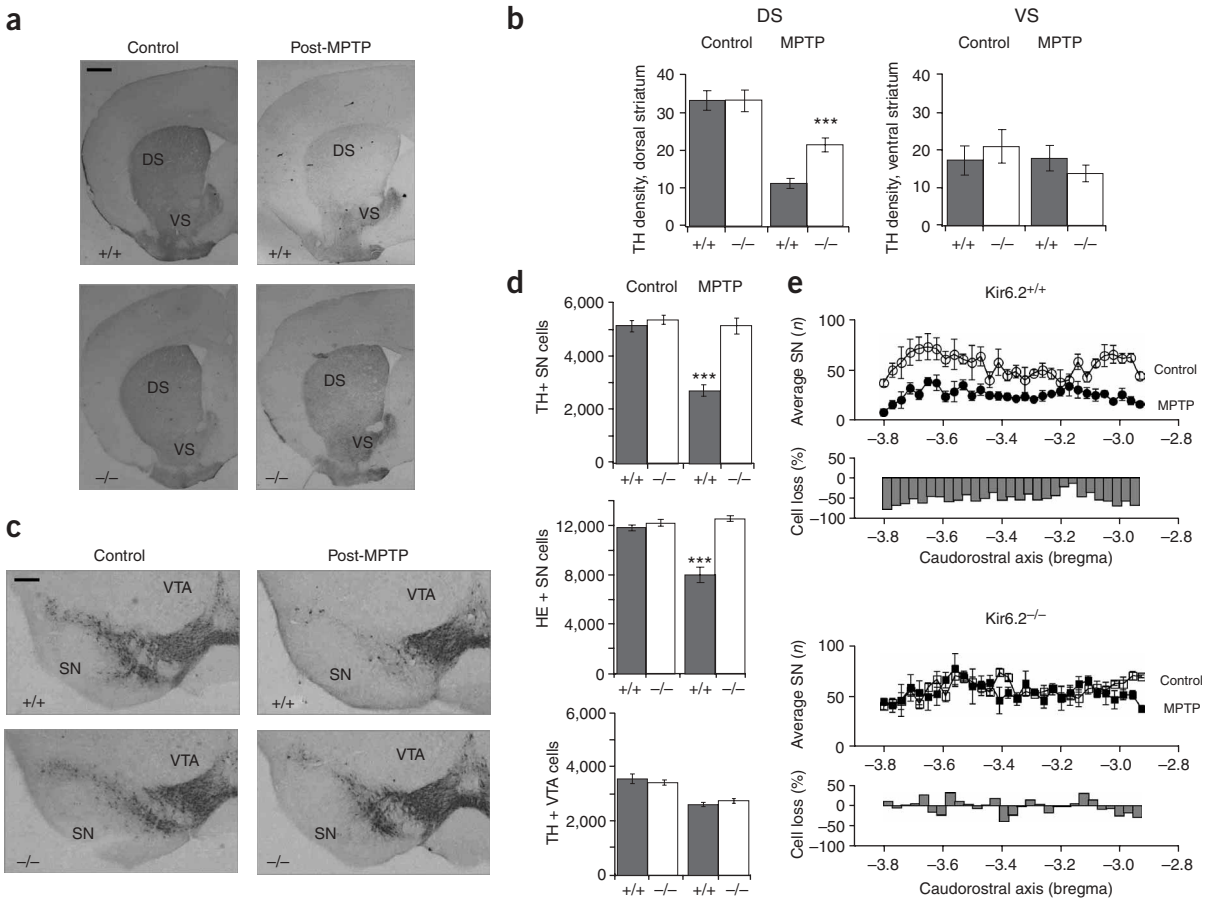

Figure 6 Selective rescue of SN DA neurons in Kir6.2$^{-/-}$ in a MPTP model of Parkinson disease. (**a**) TH immunostaining of striatal sections. Preferential post-MPTP loss of TH immunostaining in dorsal striatum (DS) but not ventral striatum (VS) of Kir6.2$^{+/+}$ mice but not Kir6.2$^{-/-}$ mice (scale bar, 1 mm). (**b**) Optical density quantification of TH immunostaining intensity of dorsal and ventral striatum of sham-injected Kir6.2$^{+/+}$ and Kir6.2$^{-/-}$ controls and post-MPTP Kir6.2$^{+/+}$ and Kir6.2$^{-/-}$ mice. (**c**) TH immunostaining of midbrain section from control and MPTP-treated Kir6.2$^{+/+}$ and Kir6.2$^{-/-}$ mice. Selective loss of TH-immunostained cells in SN of Kir6.2$^{+/+}$ mice (scale bar, 200 μm). (**d**) Nonbiased stereological analysis of TH-immunopositive and hematoxylin–eosin–positive cells in SN (top and center) and TH-immunopositive cells in VTA (bottom) from control and MPTP-treated Kir6.2$^{+/+}$ and Kir6.2$^{-/-}$ mice. Note complete rescue of DA SN cells in Kir6.2$^{-/-}$ mice. (**e**) Upper panels: average number of unbiased sampled TH-positive SN neurons in 30 serial midbrain sections, covering the caudo-rostral axis (bregma –3.8 to –3.2) in control and MPTP-treated Kir6.2$^{+/+}$ and Kir6.2$^{-/-}$ mice. Lower panels: average loss (%) of TH-positive SN neurons along the caudo-rostral axis. Note absence of cell loss throughout the entire caudorostral extent of the SN in Kir6.2$^{-/-}$ mice.

loss of TH-positive neurons in the VTA after chronic MPTP treatment (Kir6.2$^{-/-}$ VTA: control, 3,438 ± 90, $n = 5$; post-MPTP, 2,755 ± 89, $n = 4$; $P = 0.001$) was not significantly different between Kir6.2$^{-/-}$ and wild-type mice. Notably, however, we found no evidence for cell loss of TH-positive SN neurons in Kir6.2$^{-/-}$ after MPTP treatment (SN: control, 5,408 ± 172, $n = 6$; post-MPTP, 5,179 ± 285, $n = 5$; $P = 0.5$). Compared with Kir6.2$^{+/+}$ mice ($P = 1.1 \times 10^{-7}$), we detected a complete and selective rescue of the highly vulnerable population of DA neurons in the SN across the entire caudo-rostral extent of the midbrain in Kir6.2$^{-/-}$ mice (**Fig. 6d**,**e**, bottom). Stereological analysis of all SN pars compacta neurons in hematoxylin-eosin counterstained sections demonstrated genuine MPTP-induced neuronal death in wild-type mice and confirmed the complete rescue of SN neurons in the Kir6.2$^{-/-}$ mice (**Fig. 6d**, middle panel; Kir6.2$^{+/+}$ SN: control, 11,882 ± 222; post-MPTP, 8,061 ± 632, $P = 0.029$; Kir6.2$^{-/-}$ SN: control, 12,288 ± 231; post-MPTP, 12,619 ± 223; $P = 0.36$; $n = 3$ each).

Striatal MPP+ levels 90 min after MPTP injection were not significantly different between wild-type and knockout mice (Kir6.2$^{+/+}$: 16.0 ± 0.96 μM, $n = 10$; Kir6.2$^{-/-}$: 21.3 ± 2.4 μM, $n = 11$; $P = 0.06$). We also measured striatal TH fiber density (**Fig. 7b**), and striatal dopamine and 3,4-dihydroxyphenylacetic acid (DOPAC) levels (**Fig. 7c**) before and 3.5 d after MPTP injections. These experiments excluded potentially confounding differences between Kir6.2$^{-/-}$ and Kir6.2$^{+/+}$ mice in MPTP metabolism, dopamine metabolism, or acute dopamine depletion after MPTP injection. In contrast, the mesostriatal system of Kir6.2$^{-/-}$ mice seemed more vulnerable after only a single MPTP injection. TH fiber density was significantly reduced ($P = 0.004$) in the dorsal striatum of Kir6.2$^{-/-}$ mice (**Fig. 7b**; dorsal striatum control: Kir6.2$^{+/+}$, 33.0 ± 3.0; Kir6.2$^{-/-}$, 32.0 ± 2.8; dorsal striatum post-MPTP: Kir6.2$^{+/+}$, 28.3 ± 3.4, Kir6.2$^{-/-}$, 20.8 ± 1.2; ventral striatum control: Kir6.2$^{+/+}$, 26.4 ± 4.0; Kir6.2$^{-/-}$, 22.5 ± 4.0; ventral striatum post-MPTP: Kir6.2$^{+/+}$, 27.0 ± 5.5; Kir6.2$^{-/-}$, 27.6 ± 3.7; $n = 6$ each). In addition, striatal levels of dopamine and dopamine/DOPAC ratios were slightly lower in Kir6.2$^{-/-}$ mice than in controls after one dose of MPTP (**Fig. 7c**; dopamine controls (ng g^{-1}): Kir6.2$^{+/+}$, 6,869 ± 714; Kir6.2$^{-/-}$, 6,292 ± 432, $n = 10/10$; post-MPTP: Kir6.2$^{+/+}$, 4,120 ± 565; Kir6.2$^{-/-}$, 2,166 ± 217, $n = 10$ (Kir6.2$^{+/+}$) and $n = 6$ (Kir6.2$^{-/-}$); $P = 0.02$; control dopamine/DOPAC ratio: Kir6.2$^{+/+}$, 19.1 ± 0.7;

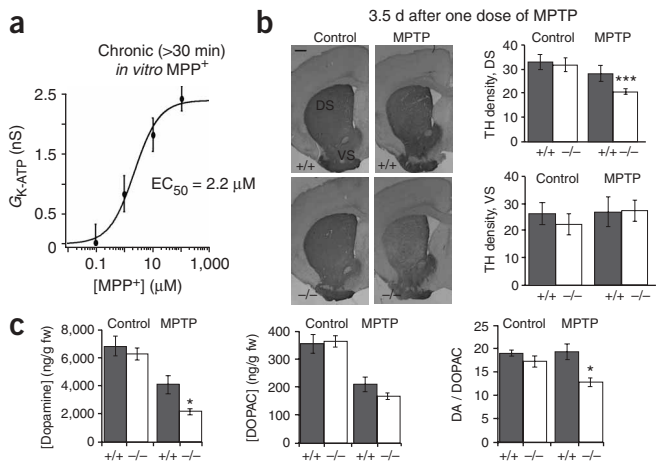

Figure 7 *In vitro* responses to MPP+ and short-term *in vivo* responses to MPTP in Kir6.2$^{+/+}$ and Kir6.2$^{-/-}$ mice. (**a**) MPP+ concentration–dependence of K-ATP channel conductance ($G_{K\text{-}ATP}$) in DA SN neurons. Points are mean ± s.e.m. of four to eight experiments. Line represents a fit of the mean data by a Hill equation with a half-maximal effective concentration (EC_{50}) of 2.2 μM and a Hill coefficient of 1. (**b**) Left: TH immunostaining of striatal sections from Kir6.2$^{+/+}$ and Kir6.2$^{-/-}$ controls and Kir6.2$^{+/+}$ and Kir6.2$^{-/-}$ mice 3.5 d after a single injection of MPTP (scale bar, 1 mm). Right: optical density quantification of TH immunostaining intensity of dorsal striatum and ventral striatum (compare with **Fig. 4a**). (**c**) Mean concentrations of dorsal striatal dopamine, DOPAC and DA/DOPAC ratios in Kir6.2$^{+/+}$ and Kir6.2$^{-/-}$ controls and 3.5 d after a single MPTP injection. There was significant DA depletion after a single MPTP injection in both Kir6.2$^{+/+}$ and Kir6.2$^{-/-}$ mice.

Kir6.2$^{-/-}$, 17.3 ± 1.2; post-MPTP: Kir6.2$^{+/+}$, 19.4 ± 1.7; Kir6.2$^{-/-}$, 12.8 ± 0.9; $P = 0.01$). In both Kir6.2$^{+/+}$ and Kir6.2$^{-/-}$ mice, DA depletion and TH fiber loss were reversible 1 week after injection (data not shown). Higher TH fiber loss and lower striatal dopamine level after one MPTP injection is in accordance with the well-described acute neuroprotective effect of K-ATP channel activation in response to metabolic stress[28,36–39]. Despite the loss of the acute neuroprotective effect in the Kir6.2$^{-/-}$ mice, genetic inactivation of K-ATP channels leads to selective and complete rescue of vulnerable SN DA neurons in the MPTP mouse model of Parkinson's disease.

Selective SN DA rescue in Kir6.2$^{-/-}$ *weaver* double mutants

To investigate whether K-ATP channel activation is a general mechanism beyond the constraints of MPTP models, we analyzed an additional genetic model of selective dopaminergic degeneration, the *weaver* (*wv/wv*) mouse[35]. Owing to a point mutation in the *Girk2* gene (Kir3.2, KCNJ6), homomeric Girk2 channels lose their potassium selectivity and G protein control and become constitutively active channels. Consequently, in homozygous *weaver* mice, dopaminergic midbrain neurons are affected by selective degeneration[25,35]. In addition, the cerebellum of homozygous *weaver* mice is markedly reduced in size, owing to a loss of cerebellar granule cells[40]. We have previously shown that K-ATP channels containing SUR1 and Kir6.2 subunits are activated in SN DA midbrain neurons of homozygous *weaver* mice in response to active *weaver* mutant channels during the most active phase of postnatal DA degeneration[25]. Here, to study the effect of loss of K-ATP channels on dopaminergic degeneration in *weaver* mice *in vivo*, we crossed heterozygote *weaver* mice (*wv*/+) with Kir6.2$^{-/-}$ mice to generate *weaver* Kir6.2$^{+/+}$ (*wv/wv* Kir6.2$^{+/+}$) and *weaver* Kir6.2$^{-/-}$ mice (*wv/wv* Kir6.2$^{-/-}$) and control mice of similar genetic background (*wv*$^{+/+}$ Kir6.2$^{+/+}$ and *wv*$^{+/+}$ Kir6.2$^{-/-}$).

The cerebella of adult 3-month-old homozygous *weaver* mice were both significantly reduced in size, regardless of the presence (*wv/wv* Kir6.2$^{+/+}$) or absence (*wv/wv* Kir6.2$^{-/-}$) of functional K-ATP channels (data not shown), indicating that Kir6.2 K-ATP channels did not affect cell death of cerebellar granule cells. In contrast, lack of K-ATP channels in adult *weaver* mice (*wv/wv* Kir6.2$^{-/-}$) led to partial but selective rescue of mesostriatal DA neurons. Comparison of striatal TH fiber density in *wv/wv* Kir6.2$^{+/+}$ mice with that in *wv*$^{+/+}$ Kir6.2$^{+/+}$ mice confirmed the previously described pattern of differential vulnerability (dorsal striatum versus ventral striatum, **Fig. 8a,b**)[35]. This pattern was also similar to that of the chronic MPTP mouse model (compare **Fig. 6a,b**). Optical density of TH-positive fibers of homozygous double mutant mice (*wv/wv* Kir6.2$^{-/-}$) was about 100% higher ($P = 0.005$) than that of *weaver* mice with functional K-ATP channels (*wv/wv* Kir6.2$^{+/+}$) in the dorsal striatum, but not in the ventral striatum, similar to our MPTP model mice (**Fig. 8a,b**; dorsal striatum: *wv*$^{+/+}$

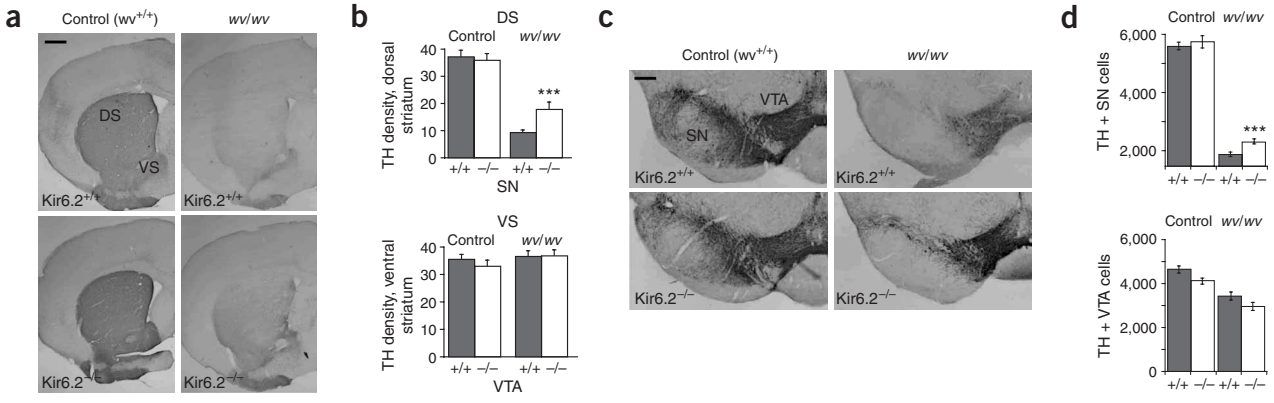

Figure 8 Selective rescue of SN DA neurons in Kir6.2$^{-/-}$ *weaver* double mutant mice. (**a**) TH immunostaining of striatal sections. There is preferential loss of TH immunostaining in dorsal striatum (DS) but not ventral striatum (VS) of *wv/wv* Kir6.2$^{+/+}$ mice but not *wv/wv* Kir6.2$^{-/-}$ mice (scale bar, 1 mm). (**b**) Optical density quantification of TH immunostaining intensity of dorsal striatum and ventral striatum of control (*wv*$^{+/+}$) and homozygous *weaver* (*wv/wv*) mice. (**c**) TH immunostaining of midbrain section from control (*wv*$^{+/+}$) and homozygous *weaver* mice either in Kir6.2$^{+/+}$ or Kir6.2$^{-/-}$ mice. Note selective loss of TH-immunostained cells in SN of *wv/wv* Kir6.2$^{+/+}$ mice (scale bar, 200 μm). (**d**) Nonbiased stereological analysis of TH-immunopositive cells in SN and VTA from control and *weaver* Kir6.2$^{+/+}$ and Kir6.2$^{-/-}$ mice. Note partial rescue of DA SN cells in *wv/wv* Kir6.2$^{-/-}$ mice.

Kir6.2$^{+/+}$, 38.0 ± 2.4; *wv/wv* Kir6.2$^{+/+}$, 9.4 ± 0.6; *wv*$^{+/+}$ Kir6.2$^{-/-}$, 36.7 ± 2.5; *wv/wv* Kir6.2$^{-/-}$, 18.2 ± 2.8; $n = 5$ each; ventral striatum: *wv*$^{+/+}$ Kir6.2$^{+/+}$, 36.1 ± 1.9; *wv/wv* Kir6.2$^{+/+}$, 37.3 ± 2.1; *wv*$^{+/+}$ Kir6.2$^{-/-}$, 33.6 ± 2.1; *wv/wv* Kir6.2$^{-/-}$, 37.5 ± 2.2; $n = 5$ each).

Stereological analysis of TH-positive midbrain neurons and of respective hematoxylin-eosin–counterstained midbrain sections confirmed the differential loss of SN DA midbrain neurons and their selective, but only partial, rescue by genetic inactivation of K-ATP channels (**Fig. 8c,d**), in contrast to the MPTP model. The number of TH-positive neurons in SN or VTA from adult 3-month-old mice did not differ in wild-type control mice (*wv*$^{+/+}$ Kir6.2$^{+/+}$) and Kir6.2$^{-/-}$ control mice (*wv*$^{+/+}$ Kir6.2$^{-/-}$). Loss of SN DA neurons in homozygous *weaver* mice was about 70% (*wv*$^{+/+}$ Kir6.2$^{+/+}$: 5,415 ± 131, $n = 3$; *wv/wv* Kir6.2$^{+/+}$: 1,687 ± 83, $n = 5$; $P = 2.4 \times 10^{-7}$). VTA DA neurons were significantly less affected by the *weaver* mutation, similar to the MPTP model; only ~25% of VTA DA neurons were lost (*wv*$^{+/+}$ Kir6.2$^{+/+}$: 4,696 ± 152, $n = 3$; *wv/wv* Kir6.2$^{+/+}$: 3,472 ± 185, $n = 5$; $P = 0.004$, *wv*$^{+/+}$ Kir6.2$^{-/-}$: 4,157 ± 155, $n = 4$; *wv/wv* Kir6.2$^{-/-}$: 2,997 ± 185, $n = 4$; $P = 0.003$). Again, moderate cell death of VTA DA neurons in mutant *weaver* mice was not affected by loss of K-ATP channels: the number of surviving VTA DA neurons did not significantly differ between Kir6.2$^{-/-}$ and Kir6.2$^{+/+}$ *weaver* mice ($P = 0.12$). In contrast, and in accordance with the MPTP model, the number of surviving SN DA neurons in double-mutant mice (*wv*$^{+/+}$ Kir6.2$^{-/-}$: 5,558 ± 203, $n = 5$; *wv/wv* Kir6.2$^{-/-}$: 2,126 ± 90, $n = 5$; $P = 3.1 \times 10^{-7}$) was significantly higher than in *wv/wv* Kir6.2$^{+/+}$ mice ($P = 0.007$), indicating that in the *weaver* mutant mice as well, genetic inactivation of the Kir6.2 gene resulted in a selective rescue of ~25% of highly vulnerable SN DA neurons. Again, analysis of hematoxylin-eosin–counterstained sections confirmed genuine cell death and rescue (SN: *wv*$^{+/+}$ Kir6.2$^{+/+}$, 11,753 ± 82; *wv*$^{+/+}$ Kir6.2$^{-/-}$, 12,328 ± 295; *wv/wv* Kir6.2$^{+/+}$, 5,387 ± 174; *wv/wv* Kir6.2$^{-/-}$: 6,568 ± 66; $n = 3$ each).

DISCUSSION

We demonstrate here that Kir6.2-containing K-ATP channels are causally linked to the differential degeneration of dopaminergic midbrain neurons *in vivo* in response to complex I inhibition as well as in response to mutant *weaver* Girk2 channels. In these two mechanistically unrelated, chronic mouse models of dopaminergic degeneration, the presence of functional K-ATP channels promotes cell death of SN DA but not VTA DA neurons. In both models, because the moderate loss of VTA DA neurons is independent of the presence of K-ATP channels, cell death of SN and VTA DA neurons is executed via divergent pathways. We have demonstrated in *in vitro* brain slices that selective K-ATP channels are selectively activated and electrical activity is lost in response to complex I inhibition in highly vulnerable SN DA neurons but that they are not activated in VTA DA neurons. Our mouse model data strongly suggest that distinct pathophysiological trigger factors (such as complex I inhibition in the MPTP model or constitutive activity of sodium-permeable mutant Girk2 channels in *weaver* mice[25]) might also converge *in vivo* on the selective activation of K-ATP channels in SN DA neurons, resulting in functional silencing. As about 70% of SN DA neurons are lost in adult *weaver* mice, it is likely that *weaver* SN DA neurons that we had previously studied in young (P14) mice[25], might not have been long-term survivors, but rather neurons in the process of degeneration. Our *in vivo* animal data indicate that functional K-ATP channels are indeed necessary for cell death of SN DA neurons in the chronic MPTP model and promote neuronal death in the mutant *weaver* mouse. As we studied a general Kir6.2 knockout mouse, we cannot rule out a contribution from Kir6.2-expressing cell types other than SN DA neurons. However, this would imply K-ATP channel activation in these other cells in the MPTP model as well as in the *weaver* mouse and selective interaction of these cells with SN DA neurons but not VTA DA neurons.

K-ATP channels are selectively activated in response to complex I inhibition in SN DA neurons but not in VTA DA neurons; this is unexpected, as adult VTA DA neurons have functional K-ATP channels with the same molecular make-up. However, given the ubiquitous expression of K-ATP channels containing Kir6.2 and SUR1 subunits, as well as their distinct physiological functions in brain and other tissues[15,16,41], cell-specific differences in K-ATP channel regulation are expected. Our results suggest that differential degrees of uncoupling of the mitochondrial respiratory chain are critical for the control of K-ATP channel activity in DA midbrain neurons. Although extensive uncoupling *in vitro* activates K-ATP channels in all DA neurons, we have found that mild uncoupling has opposite effects on K-ATP channel activity in response to complex I inhibition: it causes decreased K-ATP conductances in SN DA neurons but increased K-ATP channel conductances in VTA DA neurons. The latter express higher mRNA levels of the uncoupling protein UCP-2. In accordance, mild uncoupling has been shown to predominantly reduce generation of ROS[31], and decreased ROS will reduce the open probability of K-ATP channels[20]. Accordingly, our data suggest that the differential activation of Kir6.2- and SUR1-containing K-ATP channels in response to complex I inhibition is controlled upstream by different degrees of mitochondrial uncoupling in SN DA and VTA DA neurons. Mild basal uncoupling in VTA DA neurons seems well suited to prevent K-ATP channel activation in response to complex I inhibition, as further uncoupling by FCCP in these neurons enhances K-ATP channel activation. These findings also suggest that the neuroprotective effects of increased mitochondrial uncoupling (owing to increased levels of UCP-2 or coenzyme Q) in rodent and primate models of Parkinson disease[33,42] might act by reducing the open probability of K-ATP channels in vulnerable SN DA neurons. In essence, the convergence of mitochondrial complex I dysfunction and oxidative stress (both of which are present in Parkinson disease) on the activity of K-ATP channels provides a previously unknown candidate mechanism for differential vulnerability of DA neurons that would couple metabolic stress with electrophysiological failure and selective death of SN DA neurons.

While we have identified a mitochondrial upstream mechanism for differential K-ATP channel control in response to complex I inhibition, our study did not address downstream events that could link K-ATP channel–mediated electrical changes with death of DA neurons. Future studies must show to what extent K-ATP channel activation does occur *in vivo*, and if resulting electrical changes (such as reduced activity or functional silencing) are sufficient to kill mature DA neurons in a cell-autonomous fashion, as recently reported for maturing DA neurons *in vitro*[43]. Alternatively, functional silencing and lack of dopamine release could generate additional network effects, such as imbalances of synaptic inputs in the intact brain, that might eventually cause the death of DA neurons. However, dopamine production and release itself is not required for survival of DA neurons *in vivo*[44].

Given the well-documented function of Kir6.2-containing K-ATP channel activation in protecting complex brains against short-term stressors[28,36–39], our findings define a previously unknown role for K-ATP channels in dopaminergic pathophysiology: the promotion of long-term neurodegenerative processes. Accordingly, factors that increase K-ATP channel open probability might be beneficial during short-term metabolic demands but could also promote chronic disease. Indeed, in type 2 diabetes, the insufficient closure of β cell K-ATP channels, which control insulin secretion, is a key event[17,45]. Conse-

quently, K-ATP channel polymorphisms or a diabetic metabolic state might predispose individuals to Parkinson disease. In light of this, it is notable that early studies suggested a high prevalence of impaired glucose tolerance in Parkinson disease and exacerbation of this impairment by conventional pharmacotherapy for Parkinson disease (reviewed in ref. 46), although more recent evidence is missing. Thus, in the future, cell type–specific drugs might selectively enhance mitochondrial uncoupling or inhibit K-ATP channel activity for neuroprotection, but a clinical correction of a potential diabetic metabolic state in Parkinson disease patients might provide an already available neuroprotective strategy.

METHODS

Animals and MPTP treatment. Kir6.2$^{-/-}$ and control (Kir6.2$^{+/+}$) mice were generated and back-crossed into C57Bl/6 mice as described[26]. Homozygous *weaver* (*wv/wv* Kir6.2$^{-/-}$) and wv$^{+/+}$ Kir6.2$^{-/-}$ control mice were obtained by crossing Kir6.2$^{-/-}$ and heterozygous *weaver* mice (B6CBACa-Aw-J/A-wv, Jackson Laboratory). Genotyping for the *weaver* mutation and the Kir6.2$^{-/-}$ construct was performed by PCR after DNA isolation from small ear punches (QiaAmp DNA Mini Kit, Qiagen). Unless otherwise stated, 3-month-old male mice were used. The chronic MPTP intoxication protocol similar to that described previously[8]: 20 mg kg^{-1} MPTP in 5 mg ml^{-1} saline was injected subcutaneously, and 250 mg kg^{-1} probenecid in DMSO was injected intraperitoneally every 3.5 d over a period of 5 weeks. Mice were killed 1 week after the final injection. For acute MPTP effects, a single dose was injected. Procedures were approved by the UK Home Office and the German Regierungspräsidium Giessen. MPTP handling and safety were accordance to published safety guidelines.

Retrograde tracing and immunohistochemistry. Under stereotactic control (Cartesian Instruments), 100 nl retrobeads (Lumafluor) were injected in dorsal striatum (bregma: 0.98 mm, lateral: 1.9 mm, ventral: 2.2 mm) or nucleus accumbens (bregma: 1.54 mm, lateral: 1.0 mm, ventral: 4.0 mm) of mice under general ketamine-domitor anaesthesia. After 1 week recovery, animals were sacrificed and injection sites verified. Perfusion-fixation, immunocytochemical experiments and confocal analysis were as described previously[22]. TH-stained midbrain and control sections were rehydrated and hematoxylin-eosin counterstained (Hematoxiline-Eosine Quick Stain, Vector Labs), dehydrated and coverslipped for further stereological analysis. Optical density of striatal TH immunoreactivity was analyzed using digital imaging software (Neurolucida, MicroBrightField, Adobe Photoshop and IGOR Wavemetrics).

Stereological analysis. Total numbers of TH-positive or hematoxylin-eosin–positive neurons in SN and VTA were determined using an unbiased optical fractionator method (Stereoinvestigator, MicroBrightField). Regions of interests (SN and VTA) were identified according to established anatomical landmarks (Paxinos mouse brain atlas). We analyzed 30 serial 30-µm TH-immunostained sections (with or without hematoxylin-eosin counterstaining) from control and MPTP-treated mice as well as from double-mutant homozygous *wv/wv* Kir6.2$^{-/-}$ and *wv/wv* Kir6.2$^{+/+}$ mice and appropriate *wv*$^{+/+}$ Kir6.2$^{-/-}$ and *wv*$^{+/+}$ Kir6.2$^{+/+}$ controls, covering the entire caudo-rostral extent of the midbrain. Actual section thickness after mounting and shrinking was consistently about 11 µm. Estimated total number of TH-positive neurons (N) was calculated as follows:

$$N = \sum Q^{-} \times \frac{t}{h \times asf \times ssf}$$

where h is the height of optical dissector (5 µm), ssf is the section sampling fraction (1), asf is the area sampling fraction (0.69), t is the mean section thickness, and $\sum Q^{-}$ is the sum of counted neurons for all sections[47]. Sampling grid dimension were 120 × 120 × 5 µm (x, y and z-axes). Quality of estimated total numbers was assessed according to the Gundersen coefficient of error CE2 and was in all cases ≤ 0.05.

High-performance liquid chromatography (HPLC). For quantification of MPP+ with HPLC with fluorescence detection, striatal punches (~5 mg) were sonicated (Bandelin Sonoplus HD 70, with a Microtip) for 1 s in 20 volumes of ice-cold 5% trichloroacetic acid and centrifuged. Supernatant aliquots of 10 µl were separated over a 5-µm Sulpelcosil LC-SCX column (25 × 0.46 cm) with mobile phase of 10% ACN, 90% 0.1 M acetic acid and 0.075 M triethylamine HCl, pH 2.3, and flow rate of 1 ml min^{-1}. Eluate was monitored by a Merck-Hitachi fluorescence detector F-1000 at 295 nm excitation and 375 nm emission. Peaks were quantified by peak height evaluation and by area integration with Millennium evaluation software (Millipore). For quantification of DA and DOPAC by HPLC with electrochemical detection, brain tissues were homogenized in 40 volumes of the mobile phase, and detection was essentially as described previously[48].

Electrophysiological recordings from adult mouse brain slices. Coronal midbrain slices (250 µm) of adult mice were sectioned after intracardial perfusion with ice-cold sucrose–artificial cerebrospinal fluid (ACSF) (in mM: 50 sucrose, 75 NaCl, 25 $NaHCO_3$, 2.5 KCl, 1.25 NaH_2PO_4, 0.1 $CaCl_2$, 6 $MgCl_2$, and 2.5 glucose, oxygenated with 95% O_2/5% CO_2). After 90 min of recovery, slices were transferred to a recording chamber and perfused continuously at 2–4 ml min^{-1} with oxygenated ACSF (2.5 mM glucose, 22.5 mM sucrose) at 36 °C. Fast excitatory and inhibitory synaptic transmission was inhibited by 20 µM CNQX (6-cyano-7-nitroquinoxaline-2,3-dione) and 10 µM gabazine. Labeled SN and VTA DA neurons were visualized by infrared–differential interference contrast (IR-DIC) video microscopy and epifluorescence for detection of retrobeads[21]. Whole-cell and perforated-patch recordings, data acquisition and analysis were essentially as described[22]. Minimal subthreshold slope conductances (G_{min}) of DA neurons were determined by fitting the linear slope conductance in the subthreshold range between –50 and –70 mV of membrane currents in response to 1-s voltage ramps from –30 to –120 mV after a 200-ms conditioning step to –30 mV. Concentration-conductance data for rotenone (or MPP+) were fitted according to the Hill relationship:

$$G = G_{base} + (G_{max} - G_{base}) / (1 + (EC_{50} / [rotenone] \times n)$$

where n is the Hill coefficient and [rotenone] is the concentration of rotenone in nM.

Laser microdissection. A photoablation and laser microdissection system with fluorescence option (PALM) was used. Serial coronal cryosections (8–12 µm) of mouse midbrains were cut using a Leica cryostat CM1850 and mounted on RNAse-free ultraviolet light–treated membrane slides (1 mm polyethylene-naphthalate membrane, PALM). Sections were fixed with ethanol (four washes with 75%, 95% 100%, 100%, respectively), optionally stained with cresyl violet in 100% ethanol, and dried. Fluorescence-labeled neurons were visualized (63× objective) and marked under fluorescence illumination (rhodamine filter, 555 nm excitation) and were cut and catapulted under bright-field DIC microscopy. Individual neurons or cell pools were catapulted directly into an adhesive cap (PALM). A mixture for cell lysis (0.5% Nonidet P40, Roche Diagnostics, and 20 U SUPERaseIn, Ambion) and cDNA synthesis was added directly into the lid, the tube was incubated upside-down for 90 s at 65 °C, and the tube was quickly cooled on ice before adding reverse transcriptase.

RT-PCR. cDNA synthesis and qualitative and quantitative real-time single-cell PCR were essentially as described[49]. For multiplex PCR, HotstarTaq (Qiagen) was used, and for nested PCR, RedTaq (Sigma) was used. Primer sequences for SUR1, SUR2, calbindin D28k, TH, and GAD67 were as described[25]; primers for GAD65 were 166-CATACGCAGACAGCACGTTT (F1), 1070-AAAAGATTCC ATCGCCAGAG (R1), 606-GGGATGTCAACTACGCGTTT (F2), 994-CAC AAATACAGGGGCGATCT (R2). For quantitative real-time PCR, a 10% aliquot of cDNA from laser-microdissected cell pools was used for qualitative multiplex nested PCR to confirm marker expression (TH and CBd28k for DA neurons) and to exclude possible contamination by glial cells (as detected by glial fibrillary acidic protein (GFAP) signal) or GABAergic neurons (as detected by GAD65/GAD67 signals). All real-time Taqman assays were predesigned by Applied Biosystems and labeled with FAM as a reporter and a nonfluorescent quencher. Several assays were tested to choose those with the best performance and reproducibility, as indicated by low standard deviation for replicates with serial dilutions of control cDNA over four orders of magnitude for generation

of standard curves[49] This strategy was crucial for real-time single-cell analysis. UCP-3 was routinely detected in mouse brain cDNA (standard curve: slope = –3.06, $R^2 = 0.992$) but not in DA neurons.

Statistics. All data are given as mean ± s.e.m. To evaluate statistical significance, we used Student's *t*-tests. Normal, parametric data were compared by a two-tailed, unpaired *t*-test. A value of $P < 0.05$ was considered to be statistically significant and is indicated by *.

Accession codes. GenBank: GAD65, NM_008078.1. Applied Biosystems identifying assay identifiers: SUR1/ABCC8, Mm00803450_m1; SUR2/ABCC9, Mm00441638_m1; Kir6.1/KCNJ8, Mm00434620_m1; Kir6.2/KCNJ11, Mm00440050_s1; UCP-2, Mm00495907_g1, UCP-3, Mm00494074_m1.

ACKNOWLEDGMENTS

We are grateful to F.M. Ashcroft and R. Veh for support. We thank the animal facility of Marburg University for animal care and J. Clark, D. Meyer, E. Naudascher and H. Neuhoff for technical support. This work was supported by the Parkinson's Disease Society, UK, the Medical Research Council, Bundesministerium fuer Bildung und Forschung (BMBF-NGFNII), Gemeinnützige Hertie Foundation, Royal Society, Deutsche Forschungsgemeinschaft (J.W.), and fellowships from New College, Oxford and the Royal Society (B.L.) and Exeter College, Oxford (J.R.).

AUTHOR CONTRIBUTIONS

B.L. performed molecular biology and animal model work; O.H. performed stereological analysis; J.W. performed HPLC experiments; T.M & S.S. provided the Kir6.2$^{-/-}$ mouse; J.R. performed MPTP, tracing and electrophysiology experiments; and B.L. and J.R. designed the study and cowrote the ms.

COMPETING INTERESTS STATEMENT

The authors declare that they have no competing financial interests.

Published online at http://www.nature.com/natureneuroscience/
Reprints and permissions information is available online at http://npg.nature.com/reprintsandpermissions/

1. Morrison, B.M., Hof, P.R. & Morrison, J.H. Determinants of neuronal vulnerability in neurodegenerative diseases. *Ann. Neurol.* **44**, S32–S44 (1998).
2. Damier, P., Hirsch, E.C., Agid, Y. & Graybiel, A.M. The substantia nigra of the human brain. II. Patterns of loss of dopamine-containing neurons in Parkinson's disease. *Brain* **122**, 1437–1448 (1999).
3. Greenamyre, J.T. & Hastings, T.G. Biomedicine. Parkinson's-divergent causes, convergent mechanisms. *Science* **304**, 1120–1122 (2004).
4. Moore, D.J., West, A.B., Dawson, V.L. & Dawson, T.M. Molecular pathophysiology of Parkinson's disease. *Annu. Rev. Neurosci.* **28**, 57–87 (2005).
5. Dauer, W. & Przedborski, S. Parkinson's disease: mechanisms and models. *Neuron* **39**, 889–909 (2003).
6. Schapira, A.H. Causes of neuronal death in Parkinson's disease. *Adv. Neurol.* **86**, 155–162 (2001).
7. Moratalla, R. *et al.* Differential vulnerability of primate caudate-putamen and striosome-matrix dopamine systems to the neurotoxic effects of 1-methyl-4-phenyl-1,2,3,6-tetrahydropyridine. *Proc. Natl. Acad. Sci. USA* **89**, 3859–3863 (1992).
8. Petroske, E., Meredith, G.E., Callen, S., Totterdell, S. & Lau, Y.S. Mouse model of Parkinsonism: a comparison between subacute MPTP and chronic MPTP/probenecid treatment. *Neuroscience* **106**, 589–601 (2001).
9. Greene, J.G., Dingledine, R. & Greenamyre, J.T. Gene expression profiling of rat midbrain dopamine neurons: implications for selective vulnerability in parkinsonism. *Neurobiol. Dis.* **18**, 19–31 (2005).
10. Betarbet, R. *et al.* Chronic systemic pesticide exposure reproduces features of Parkinson's disease. *Nat. Neurosci.* **3**, 1301–1306 (2000).
11. Przedborski, S. & Vila, M. The 1-methyl-4-phenyl-1,2,3,6-tetrahydropyridine mouse model: a tool to explore the pathogenesis of Parkinson's disease. *Ann. NY Acad. Sci.* **991**, 189–198 (2003).
12. Langston, J.W. The etiology of Parkinson's disease with emphasis on the MPTP story. *Neurology* **47**, S153–S160 (1996).
13. Hoglinger, G.U. *et al.* Dysfunction of mitochondrial complex I and the proteasome: interactions between two biochemical deficits in a cellular model of Parkinson's disease. *J. Neurochem.* **86**, 1297–1307 (2003).
14. Testa, C.M., Sherer, T.B. & Greenamyre, J.T. Rotenone induces oxidative stress and dopaminergic neuron damage in organotypic substantia nigra cultures. *Brain Res. Mol. Brain Res.* **134**, 109–118 (2005).
15. Seino, S. & Miki, T. Gene targeting approach to clarification of ion channel function: studies of Kir6.x null mice. *J. Physiol. (Lond.)* **554**, 295–300 (2004).
16. Bryan, J., Vila-Carriles, W.H., Zhao, G., Babenko, A.P. & Aguilar-Bryan, L. Toward linking structure with function in ATP-sensitive K+ channels. *Diabetes* **53**, S104–S112 (2004).
17. Ashcroft, F. & Rorsman, P. Type 2 diabetes mellitus: not quite exciting enough? *Hum. Mol. Genet.* **13**, R21–R31 (2004).
18. Liss, B., Bruns, R. & Roeper, J. Alternative sulfonylurea receptor expression defines metabolic sensitivity of K-ATP channels in dopaminergic midbrain neurons. *EMBO J.* **18**, 833–846 (1999).
19. Liu, Y. & Gutterman, D.D. Oxidative stress and potassium channel function. *Clin. Exp. Pharmacol. Physiol.* **29**, 305–311 (2002).
20. Avshalumov, M.V., Chen, B.T., Koos, T., Tepper, J.M. & Rice, M.E. Endogenous hydrogen peroxide regulates the excitability of midbrain dopamine neurons via atp-sensitive potassium channels. *J. Neurosci.* **25**, 4222–4231 (2005).
21. Liss, B. & Roeper, J. Correlating function and gene expression of individual basal ganglia neurons. *Trends Neurosci.* **27**, 475–481 (2004).
22. Neuhoff, H., Neu, A., Liss, B. & Roeper, J.I. (h) channels contribute to the different functional properties of identified dopaminergic subpopulations in the midbrain. *J. Neurosci.* **22**, 1290–1302 (2002).
23. Jiang, C., Sigworth, F.J. & Haddad, G.G. Oxygen deprivation activates an ATP-inhibitable K+ channel in substantia nigra neurons. *J. Neurosci.* **14**, 5590–5602 (1994).
24. Mercuri, N.B. *et al.* Effects of anoxia on rat midbrain dopamine neurons. *J. Neurophysiol.* **71**, 1165–1173 (1994).
25. Liss, B., Neu, A. & Roeper, J. The weaver mouse gain-of-function phenotype of dopaminergic midbrain neurons is determined by coactivation of wvGirk2 and K-ATP channels. *J. Neurosci.* **19**, 8839–8848 (1999).
26. Miki, T. *et al.* Defective insulin secretion and enhanced insulin action in KATP channel-deficient mice. *Proc. Natl. Acad. Sci. USA* **95**, 10402–10406 (1998).
27. Tarasov, A., Dusonchet, J. & Ashcroft, F. Metabolic regulation of the pancreatic beta-cell ATP-sensitive K+ channel: a pas de deux. *Diabetes* **53**, S113–S122 (2004).
28. Lin, Y.F., Raab-Graham, K., Jan, Y.N. & Jan, L.Y. NO stimulation of ATP-sensitive potassium channels: involvement of Ras/mitogen-activated protein kinase pathway and contribution to neuroprotection. *Proc. Natl. Acad. Sci. USA* **101**, 7799–7804 (2004).
29. Lin, Y.F., Jan, Y.N. & Jan, L.Y. Regulation of ATP-sensitive potassium channel function by protein kinase A-mediated phosphorylation in transfected HEK293 cells. *EMBO J.* **19**, 942–955 (2000).
30. Baukrowitz, T. *et al.* PIP2 and PIP as determinants for ATP inhibition of KATP channels. *Science* **282**, 1141–1144 (1998).
31. Krauss, S., Zhang, C.Y. & Lowell, B.B. The mitochondrial uncoupling-protein homologues. *Nat. Rev. Mol. Cell Biol.* **6**, 248–261 (2005).
32. Brookes, P.S. Mitochondrial H(+) leak and ROS generation: an odd couple. *Free Radic. Biol. Med.* **38**, 12–23 (2005).
33. Horvath, T.L. *et al.* Coenzyme Q induces nigral mitochondrial uncoupling and prevents dopamine cell loss in a primate model of Parkinson's disease. *Endocrinology* **144**, 2757–2760 (2003).
34. Andrews, Z.B. *et al.* Uncoupling protein-2 is critical for nigral dopamine cell survival in a mouse model of Parkinson's disease. *J. Neurosci.* **25**, 184–191 (2005).
35. Roffler-Tarlov, S. & Graybiel, A.M. Weaver mutation has differential effects on the dopamine-containing innervation of the limbic and nonlimbic striatum. *Nature* **307**, 62–66 (1984).
36. Ballanyi, K. Protective role of neuronal KATP channels in brain hypoxia. *J. Exp. Biol.* **207**, 3201–3212 (2004).
37. Yamada, K. *et al.* Protective role of ATP-sensitive potassium channels in hypoxia-induced generalized seizure. *Science* **292**, 1543–1546 (2001).
38. Hernandez-Sanchez, C. *et al.* Mice transgenically overexpressing sulfonylurea receptor 1 in forebrain resist seizure induction and excitotoxic neuron death. *Proc. Natl. Acad. Sci. USA* **98**, 3549–3554 (2001).
39. Zingman, L.V. *et al.* Kir6.2 is required for adaptation to stress. *Proc. Natl. Acad. Sci. USA* **99**, 13278–13283 (2002).
40. Patil, N. *et al.* A potassium channel mutation in weaver mice implicates membrane excitability in granule cell differentiation. *Nat. Genet.* **11**, 126–129 (1995).
41. Liss, B. & Roeper, J. Molecular physiology of neuronal K-ATP channels. *Mol. Membr. Biol.* **18**, 117–127 (2001).
42. Conti, B. *et al.* Uncoupling protein 2 protects dopaminergic neurons from acute 1,2,3,6-methyl-phenyl-tetrahydropyridine toxicity. *J. Neurochem.* **93**, 493–501 (2005).
43. Salthun-Lassalle, B., Hirsch, E.C., Wolfart, J., Ruberg, M. & Michel, P.P. Rescue of mesencephalic dopaminergic neurons in culture by low-level stimulation of voltage-gated sodium channels. *J. Neurosci.* **24**, 5922–5930 (2004).
44. Zhou, Q.Y. & Palmiter, R.D. Dopamine-deficient mice are severely hypoactive, adipsic, and aphagic. *Cell* **83**, 1197–1209 (1995).
45. O'Rahilly, S., Barroso, I. & Wareham, N.J. Genetic factors in type 2 diabetes: the end of the beginning? *Science* **307**, 370–373 (2005).
46. Craft, S. & Watson, G.S. Insulin and neurodegenerative disease: shared and specific mechanisms. *Lancet Neurol.* **3**, 169–178 (2004).
47. Keuker, J.I., Vollmann-Honsdorf, G.K. & Fuchs, E. How to use the optical fractionator: an example based on the estimation of neurons in the hippocampal CA1 and CA3 regions of tree shrews. *Brain Res. Brain Res. Protoc.* **7**, 211–221 (2001).
48. Alburges, M.E., Narang, N. & Wamsley, J.K. Alterations in the dopaminergic receptor system after chronic administration of cocaine. *Synapse* **14**, 314–323 (1993).
49. Liss, B. *et al.* Tuning pacemaker frequency of individual dopaminergic neurons by Kv4.3L and KChip3.1 transcription. *EMBO J.* **20**, 5715–5724 (2001).